Accelerated evolution of convective simulations

Evan H. Anders and Benjamin P. Brown
Dept. Astrophysical & Planetary Sciences, University of Colorado – Boulder, Boulder, CO 80309, USA and Laboratory for Atmospheric and Space Physics, Boulder, CO 80303, USA

Jeffrey S. Oishi
Department of Physics and Astronomy, Bates College, Lewiston, ME 04240, USA

We present a method for achieving Accelerated Evolution (AE) of convective simulations. By probing the dynamics of convection early in simulations and adjusting the thermal profile of the simulation appropriately, we advance simulations to evolved states on timescales much shorter than the thermal diffusion timescale. We study this method in the context of Rayleigh-Bénard convection. The solutions reached by AE similar to those reached by a slow thermal evolution, and AE is effective in 2D, 3D, and at low and high supercriticality. Extensions to more complex systems are briefly discussed.

I. INTRODUCTION

Astrophysical convection occurs in the presence of disparate timescales which prohibit numericists from studying realistic models of systems in nature. For example, flows in the convection zones of stars like the Sun are characteristically low Mach number (Ma) in the deep interior. Explicit timestepping methods which are bound by the Courant-Friedrich-Lewy (CFL) timestep limit must resolve the fastest motions (sound waves), resulting in timesteps which are prohibitively small for studies of the deep, low-Ma motions. These systems are numerically stiff, and the difference between the sound crossing time and the convective overturn time have made studies of low-Ma stellar convection difficult. Traditionally, approximations such as the anelastic approximation, in which sound waves are explicitly filtered out, have been used to study low-Ma flows [1, 2]. More recently, advanced numerical techniques which use fully implicit [3–5] or mixed implicit-explicit [6–8] timestepping mechanisms have made it feasible to study convection at low Mach numbers, and careful studies of deep convection which would have been impossible a decade ago are now widely accessible.

Unfortunately, convective systems generally evolve over the course of thermal timescales, which are often much larger than all relevant dynamical timescales. Therefore resolving dynamics in atmospheres which are sufficiently thermally relaxed remains a challenging problem. Solar convection is a prime example of this phenomenon, as dynamical timescales in the solar convective zone are relatively short (convection overturns every ~ 10 minutes at the solar surface, the Sun rotates roughly once every month) compared to the Sun's Kelvin-Helmholtz timescale of $3 \cdot 10^7$ years [9]. In such a system, it is impossible to resolve the convective dynamics while also meaningfully evolving the thermal structure of the system using traditional timestepping techniques alone. As modern simulations aim to model natural convection by increasing into the high-Rayleigh-number (Ra) regime, the thermal diffusion timescale becomes intractably large compared to dynamical timescales [7]. Furthermore, as dynamical and thermal timescales separate, simulations become more turbulent. Capturing appropriately resolved turbulent motions requires finer grid meshes and smaller timesteps. Thus, the progression of simulations into the high-Ra regime of natural convection is slowed by two simultaneous effects: timestepping through a single convective overturn time becomes more computationally expensive and the number of overturn times required for systems to reach thermal equilibration grows.

The vast difference between convective and thermal timescales has long plagued numericists studying convection, and an abundance of approaches has been employed to study thermally converged solutions. One popular method for accelerating the convergence of high-Ra solutions is by "bootstrapping" – the process of using the flow fields in a converged solution at low Ra as initial conditions for a simulation at high Ra. This method has been used with great success [10, 11], but it is not without its faults. Bootstrapped solutions are susceptible to hysteresis effects, in which large-scale convective structures present in the low Ra solution imprint onto the dynamics of the new, high Ra solution. Another commonly-used tactic in moderate-Ra simulations is to use a simple model of the full convective state as initial conditions. For example, past studies have used a linear eigenvalue solve to set the initial convective state [12] or used an axisymmetric solution as initial conditions for convection in a 3D cylinder [11]. In other systems, the approximate state of the evolved solution can be estimated. There, a set of initial conditions which is close to the evolved state can be derived analytically [13, 14].

Despite the numerous methods that have been used, the most straightforward way to achieve a thermally converged solution is to evolve a convective simulation through a thermal timescale. Some modern studies do just that [2]. However, such evolution is *expensive*, and state-of-the-art simulations at the highest values of Ra can only reasonably be run for hundreds of freefall timescales [15], much less the thousands or millions freefall times required for thermal convergence.

In this work, we study a method of achieving accelerated evolution of convective simulations. We couple measurements of the dynamics of unequilibrated convective simulations with knowledge about energy balances in the desired solution to self-consistently adjust the mean vertical thermodynamic profile towards its evolved state. While a technique of this kind has been used previously [16], we find no explanation in the current literature of the steps involved in employing this method, nor do we find any study of its accuracy. In section II, we describe our convective simulations, our numerical methods, and the procedure for achieving accelerated evolution. In section III, we compare accelerated evolution solutions to solutions obtained from evolution through a full thermal diffusion timescale. Finally, in section IV, we offer concluding remarks and discuss extensions of the methods presented here.

II. EXPERIMENT

We study incompressible Rayleigh-Bénard convection under the Oberbeck-Boussinesq approximation, such that the fluid has a constant kinematic viscosity (ν), thermal diffusivity (κ), and coefficient of thermal expansion (α). The density of the fluid is a constant, ρ_0, except where it is $\rho = \rho_0(1-\alpha T_1)$ on the term where the constant gravitational acceleration, $\boldsymbol{g} = -g\hat{z}$, acts in the vertical momentum equation. The equations of motion are [17]

$$\nabla \cdot \boldsymbol{u} = 0, \tag{1}$$

$$\frac{\partial \boldsymbol{u}}{\partial t} + \boldsymbol{u}\cdot\nabla\boldsymbol{u} = -\frac{1}{\rho_0}\nabla P - g(1-\alpha T_1)\hat{z} + \nu\nabla^2\boldsymbol{u}, \tag{2}$$

$$\frac{\partial T_1}{\partial t} + \boldsymbol{u}\cdot\nabla(T_0 + T_1) = \kappa\nabla^2 T_1, \tag{3}$$

where $\boldsymbol{u} = u\hat{x} + v\hat{y} + w\hat{z}$ is the velocity, $T = T_0(z) + T_1(x, y, z, t)$ are the initial and fluctuating components of temperature, and P is the kinematic pressure. We non-dimensionalize these equations such that length is in units of the layer height (L_z), temperature is in units of the initial temperature jump across the layer ($\Delta T_0 = L_z \nabla T_0$), and velocity is in units of the freefall velocity ($v_{\text{ff}} = \sqrt{\alpha g L_z^2 \nabla T_0}$). By these choices, one time unit is a freefall time ($t_{\text{ff}} = L_z/v_{\text{ff}}$). We introduce a reduced kinematic pressure, $\varpi \equiv (P/\rho_0 + \phi + |\boldsymbol{u}|^2/2)/v_{\text{ff}}^2$, where the gravitational potential, ϕ, is defined such that $\boldsymbol{g} = -\nabla\phi$. In non-dimensional form, Eqns. 2 & 3 become

$$\frac{\partial \boldsymbol{u}}{\partial t} + \nabla\varpi - T_1\hat{z} + \mathcal{R}\nabla\times\boldsymbol{\omega} = \boldsymbol{u}\times\boldsymbol{\omega}, \tag{4}$$

$$\frac{\partial T_1}{\partial t} - \mathcal{P}\nabla^2 T_1 + w\frac{\partial T_0}{\partial z} = -\boldsymbol{u}\cdot\nabla T_1, \tag{5}$$

where $\boldsymbol{\omega} = \nabla\times\boldsymbol{u}$ is the vorticity. The dimensionless control parameters $\mathcal{R}$ and $\mathcal{P}$ are set by the Rayleigh (Ra) and Prandtl (Pr) numbers,

$$\mathcal{R} \equiv \sqrt{\frac{\text{Pr}}{\text{Ra}}}, \qquad \mathcal{P} \equiv \frac{1}{\sqrt{\text{Pr}\,\text{Ra}}}, \qquad \text{Ra} = \frac{g\alpha L_z^4 \nabla T_0}{\nu\kappa} = \frac{(L_z\, v_{\text{ff}})^2}{\nu\kappa}, \qquad \text{Pr} = \frac{\nu}{\kappa}. \tag{6}$$

We hold $\text{Pr} = 1$ constant throughout this work, such that $\mathcal{P} = \mathcal{R}$.

In Eqns. (1), (4), & (5), linear terms are grouped on the left-hand side of the equations, while nonlinear terms are found on the right-hand side. We timestep linear terms implicitly, and nonlinear terms explicitly. We utilize the Dedalus[1] pseudospectral framework [20] to evolve Eqns. (1), (4), & (5) forward in time using an implicit-explicit (IMEX), third-order, four-stage Runge-Kutta timestepping scheme RK443 [21].

Variables are time-evolved on a dealiased Chebyshev (vertical) and Fourier (horizontal, periodic) domain in which the physical grid dimensions are 3/2 the size of the coefficient grid. We study 2D and 3D convection in which the domain is a cartesian box, whose dimensionless vertical extent is $z \in [-1/2, 1/2]$, and which is horizontally periodic with an extent of $x, y \in [0, \Gamma]$, where $\Gamma = 2$ is the aspect ratio. In 2D simulations, we set $v = \partial_y = 0$. We specify no-slip, impenetrable boundary conditions at both the top and bottom boundary and we use mixed thermal boundary conditions, such that

$$u = v = w = 0 \text{ at } z = \pm 1/2, \qquad T_1 = 0 \text{ at } z = +1/2, \qquad \frac{\partial T_1}{\partial z} = 0 \text{ at } z = -1/2. \tag{7}$$

[1] http://dedalus-project.org/

For this choice of boundary conditions, the critical value of Ra at which the onset of convection occurs is $\mathrm{Ra}_{\mathrm{crit}} = 1295.78$, and the supercriticality of a run is defined as $S \equiv \mathrm{Ra}/\mathrm{Ra}_{\mathrm{crit}}$. Studies of convection which aim to model astrophysical systems such as stars often employ mixed thermal boundary conditions [12, 18, 19], as we do here; however, our choice of thermal boundary conditions here reflects the fact that the conditions in Eqn. (7) are the simplest to implement in the process of accelerated evolution (section II A) we study here.

The initial temperature profile is linearly unstable, $T_0(z) = -z$. On top of this profile, we fill T_1 with random white noise whose magnitude is $10^{-6}\mathcal{P}$. This ensures that the initial perturbations are much smaller than the evolved convective temperature perturbations, even at large Ra. We filter this noise spectrum in coefficient space, such that only the lower 25% of the coefficients have power.

A. The method of Accelerated Evolution

Here we describe a method of Accelerated Evolution (AE), which we use to rapidly evolve the thermodynamic state of convective simulations. We compare this AE method to Standard Evolution (SE), in which we naively evolve the atmosphere for one thermal diffusion time, $t_\kappa = \mathcal{P}^{-1}$. Both AE and SE simulatins begin with identical initial conditions, as described in section II. As Ra increases, and $\mathcal{P}$ decreases, SE solutions become intractable, while the timeframe of convergence for an AE solution remains nearly constant in simulation freefall time units (see table I).

For an example of time saving achieved by using AE, we compare energy traces at $S = 10^5$ from a SE run in Fig. 1a to an AE run in Fig. 1c. In Fig. 1a, the time evolution of the SE simulation is shown. The solution grows exponentially from white noise during the first $\sim 25\ t_{\mathrm{ff}}$. The solution then saturates and begins to slowly equliibrate towards the proper isothermal profile in the interior of the domain. We find that the mean atmospheric temperature and kinetic energies are fully converged when $t = 4000\ t_{\mathrm{ff}} = 0.35\ t_\kappa$. We show roughly the first thousand freefall time units of evolution, as well as the evolved thermodynamic state reached after a full thermal time of evolution. In Fig. 1c, we show an AE solution at the same parameters. The same linear growth phase occurs, but shortly after the peak of convective transient we accelerate the convergence of the atmosphere through the process which we describe below. We adjust the 1D vertical profile of the atmosphere three times, as denoted by the three labeled arrows in the graph numbered 1-3. After the third profile adjustment, we find that the atmosphere is nearly in its converged state and we can begin to sample the evolved convective dynamics.

The horizontally averaged profiles of the vertical conductive flux, $\mathrm{F}_\kappa = \langle -\kappa \nabla (T_0 + T_1) \rangle_{x,y}$, and the vertical convective enthalpy flux, $\mathrm{F_E} = \langle w(T_0 + T_1) \rangle_{x,y}$, are the basis of the AE method. Here we use $\langle \rangle_{x,y}$ to represent a horizontal average. We measure both of these fluxes early in a simulation, retrieving profiles such as those shown in Fig. 1b. At these early times, the flux profiles are highly asymmetric, with more flux exiting the atmosphere at the upper boundary than the fixed-flux lower boundary can provide. As the atmosphere evolves towards the isothermal profile specified by the upper (cold) boundary condition, excess temperature throughout the atmosphere must leave the domain, and this appears in the flux measurements in Fig. 1b where the flux exiting the upper boundary is nearly 2000% the flux entering the bottom of the domain. Once the atmospheric temperature profile reaches its evolved state, the flux entering the bottom boundary is equal to the flux exiting the upper boundary. In general, this takes very long time frames through SE (Fig. 1a), but AE (Fig. 1b) can take a system whose fluxes are in a strongly disequilibrium state (Fig. 1c), and quickly put them into a near-equilibrium state, as shown in Fig. 1d. In this final state, there is no conductive flux in the interior, both boundaries carry the same amount of flux, and convection carries that amount of flux through the interior. The converged state achieved through AE is at most 5% different from the SE solution, as shown in Fig. 1e.

In order to adjust the temperature profle to achieve AE, we calculate the total flux, $\mathrm{F_{tot}} = \mathrm{F_E} + \mathrm{F}_\kappa$, and then derive the profiles

$$f_{\mathrm{E}}(z) = \frac{\mathrm{F_E}}{\mathrm{F_{tot}}}, \qquad f_\kappa(z) = \frac{\mathrm{F}_\kappa}{\mathrm{F_{tot}}}, \tag{8}$$

which have the systematic asymmetries removed. These profiles describe which parts of the atmosphere depend on convection to carry flux (where $f_{\mathrm{E}}(z) = 1$ and $f_\kappa(z) = 0$). We presume that the early convection occupies roughly the same volume as the evolved convection, and thus that the extent of the early thermal boundary layers (where $f_\kappa(z) = 1$ and $f_{\mathrm{E}}(z) = 0$) will not change significantly over the course of the atmosphere's evolution. Under this assumption, in order to reach the converged state, the flux through the atmosphere must be decreased by some amount,

$$\xi(z) \equiv \frac{\mathrm{F_B}}{\mathrm{F_{tot}}}, \tag{9}$$

where $\mathrm{F_B} = \mathcal{P}$ is the amount of flux that enters the bottom of the atmosphere.

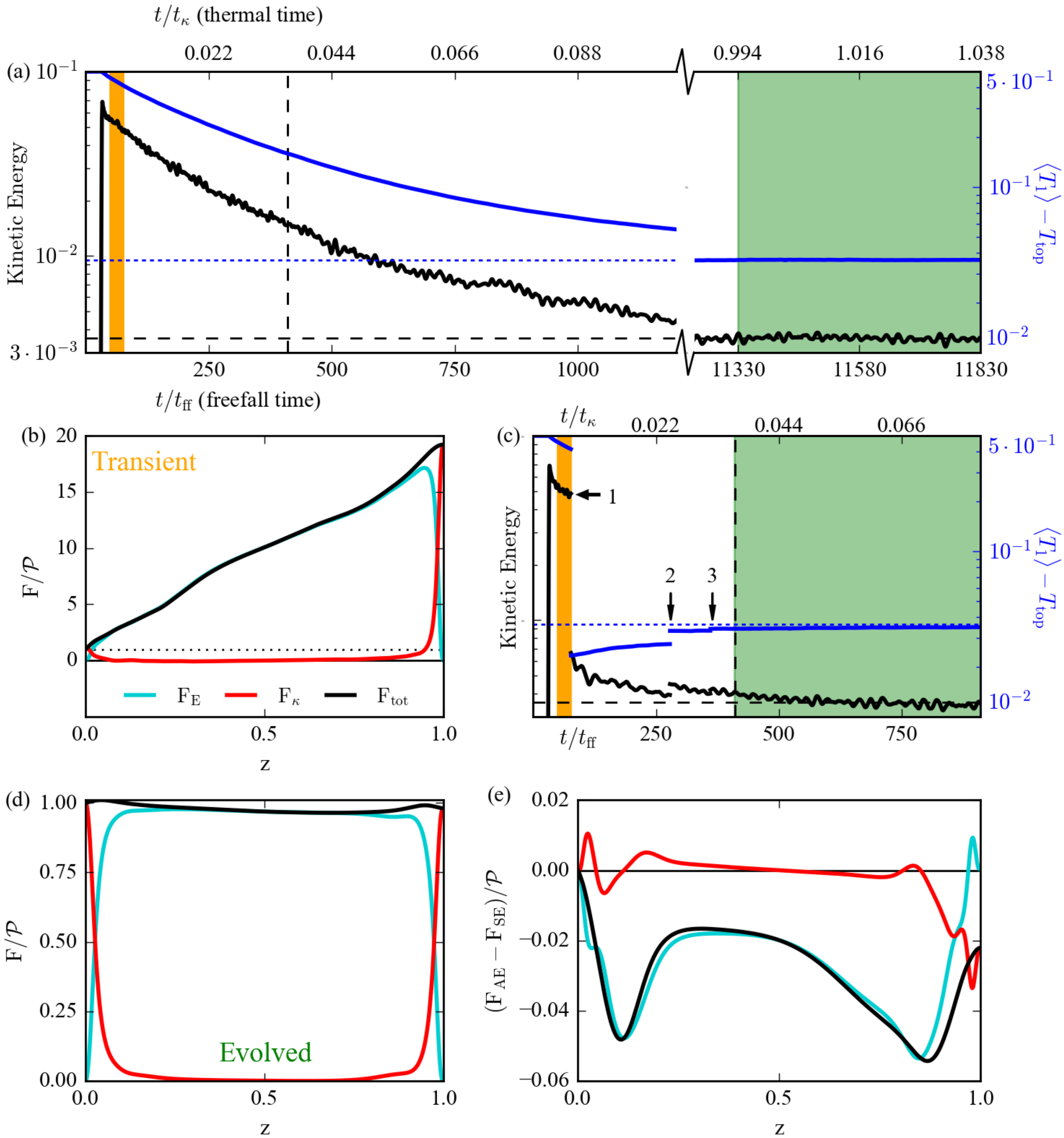

FIG. 1. (a) Kinetic energy (black) and mean temperature (blue) vs. time are shown for a SE run at $S = 10^5$. The mean evolved values of kinetic energy and mean temperature, averaged over the time shaded in green, are denoted by the horizontal dashed lines. (b) The time- and horizontally-averaged flux profiles are shown for the times highlighted in orange. (c) The same quantities as in (a) are shown, but for AE at the same parameters. The axes are scaled identically in (a) and (c), and the AE method is used three times, marked by the numbered arrows in (c). The fluxes averaged over the green shaded region of (c) are shown in (d). The difference between the fluxes in the AE and SE solutions is shown in (e).

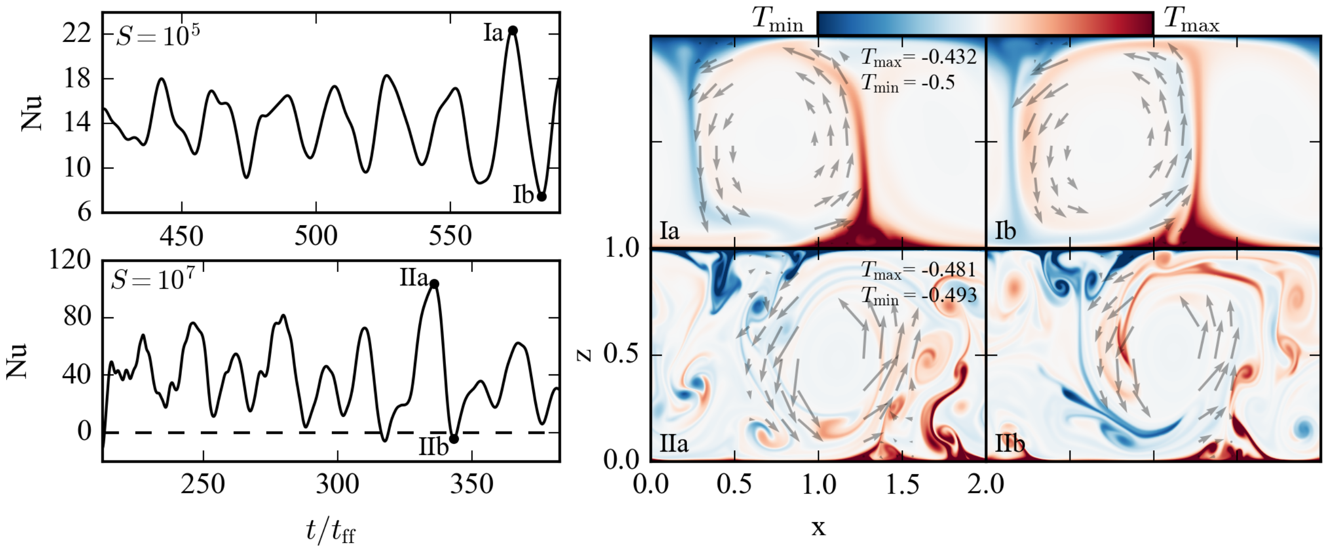

FIG. 2. .

In a time-stationary state, the horizontal- and time-average of Eqns. (4) and (5), neglecting terms which vanish due to symmetry, are

$$\frac{\partial}{\partial z} \langle \varpi \rangle_{x,y} - \langle T_1 \rangle_{x,y} \hat{z} = \langle \boldsymbol{u} \times \boldsymbol{\omega} \rangle_{x,y,\text{ ev}}\,, \tag{10}$$

$$\frac{\partial}{\partial z} \mathrm{F}_{\text{E, ev}} - \mathcal{P} \frac{\partial^2}{\partial z^2} \langle T_1 \rangle_{x,y} = 0. \tag{11}$$

Here, we construct $\langle \boldsymbol{u} \times \boldsymbol{\omega} \rangle_{x,y,\text{ ev}} = \xi(z) \langle \boldsymbol{u} \times \boldsymbol{\omega} \rangle_{x,y}$ and $\mathrm{F}_{\text{E, ev}} = \xi(z)\mathrm{F}_{\text{E}}$ from our unevolved state, and solve for $\langle \varpi \rangle_{x,y}$ and $\langle T_1 \rangle_{x,y}$. Convective flows are perturbations around a thermal profile defined by these equations in the proper evolved, statistically stationary state. Furthermore, under the specification of $\mathrm{F}_{\text{conv, ev}}$ and $\langle \boldsymbol{u} \times \boldsymbol{\omega} \rangle_{x,y}$, *the mean thermodynamic structure of the system is fully specified.*

Thus, the AE method is simple: we construct $\xi(z)$ from measured information about the convective dynamics. We solve a 1D boundary value problem consisting of Eqns. (10) & (11) to obtain the proper evolved thermodynamic profile, and proper conductive flux. To obtain the proper convective enthalpy flux, we multiply both the velocity field, $\boldsymbol{u}$, and the temperature perturbations around the mean, $T - \langle T \rangle_{x,y}$, by $\sqrt{\xi}$, thus diminishing the magnitude of these perturbations appropriately. After adjusing the fields of a simulation in this manner, we continue timestepping forward. For specifics on the precise implementation of the AE method, we refer the reader to appendix A.

III. RESULTS

We study evolved SE solutions whose supercriticalities (S) are $S \in (1, 10^5]$ in 2D and $S \in (1, 10^4]$ in 3D. We compare their properties to accelerated evolution (AE) runs in $S \in (1, 10^7]$ in 2D and $S \in (1, 10^4]$ in 3D. We refer the reader to appendix B for a full list of simulations.

The Nusselt number (Nu) quantifies the efficiency of convective heat transport and is defined as

$$\mathrm{Nu} = \frac{\langle F_{\text{conv}} + F_{\text{cond}} \rangle}{\langle F_{\text{cond, ref}} \rangle} = \frac{\langle wT - \mathcal{P}\partial_z T \rangle}{\langle -\mathcal{P}\partial_z T \rangle}, \tag{12}$$

where the volume average of a quantity, η, is shown as $\langle \eta \rangle$. When $S < 10^{3+2/3}$ in 2D and for all runs in 3D, the evolved system is characterized by a specific value of Nu, as the convective heat transport reaches a temporally stationary state. At larger values of S in 2D, the value of Nu varies significantly over time, as shown by the time traces for $S = 10^5$ (top) and $S = 10^7$ (bottom) for two AE runs in Fig. 2. We find that these systems go between states in which temperature fluctuations primarily travel in their natural buoyant direction (as in Ia and IIa, where cold elements are falling and hot elements rise), and states in which temperature perturbations are entrained in an upflow or downflow with oppositely signed fluid (as in Ib and IIb, where warm fluid is pulled down by the downflow lane, and cool fluid is pulled up by the upflow lane). The fluid from the oppositely signed plume pushes on the other plume such that the system goes between states in which the fluid primarily serves to enhance convective transport (Ia and IIa), states in which there is counterclockwise entrainment (IIa and IIb), then back to enhanced transport states followed by clockwise entrainment. This horizontally oscillatory motion that characterizes the plumes provides, and the resultant time-dependent entrainment, leads to large variations in Nu over time As a result of our choice of no-slip boundary conditions, the fluid never enters a full domain shearing state [22], and the oscillatory nature of the plumes is stable. The 2D SE simulations exhibit the same horizontally oscillatory behavior as the AE solutions for the same initial conditions. This time-dependent behavior or Nu is not seen strongly in our 3D solutions, likely as a result of the extra degrees of freedom in which rising and falling fluid elements can expand, reducing entrainment.

The time- and volume-averaged values of the Nusselt number (Nu), the RMS Reynolds number (Re), and the mean temperature in AE solutions are shown in Fig. 3a-c. Nu, which quantifies the heat transport in evolved solutions, is shown as a function of Ra and S in Fig. 3a. The dynamic nature of the plume structures diminishes the scaling of the heat transport to $\mathrm{Nu} \propto \mathrm{Ra}^{1/5}$, which is weaker than classic scaling laws [10, 23]. Previous studies in 2D convection may have avoided oscillatory plumes by using bootstrapping techniques as initial conditions for high S runs. In Fig. 3b, we report $\mathrm{Re} = \langle|\boldsymbol{u}|\rangle/\mathcal{R}$. This measures the degree of turbulence in the solution, and scales roughly as $\mathrm{Re} \propto \mathrm{Ra}^{0.45}$. Each simulation shows little variance in the value of Re over time. Fig. 3c shows the scaling of $\langle T\rangle - T_{\mathrm{top}}$. The average temperature, $\langle T\rangle$, is dominated by its value in the isothermal interior, so this measurements serves as a probe of the temperature jump across the boundary layers. As a result, we expect this measure to scale inversely with Nu in converged solutions where fixed-flux boundary conditions are used [24]. We find here that $(\langle T\rangle - T_{\mathrm{top}}) \propto \mathrm{Ra}^{-1/5}$, precisely the inverse scaling of Nu.

This is a short paragraph which says 2D and 3D are the same, here.

In Fig. 3d-f, we report the fractional difference between measurements in the AE and SE solutions. The mean values of Nu and $\langle T\rangle - T_{\mathrm{top}}$ measured in AE are accurate to SE values to within $\sim 1\%$. Re measurements show

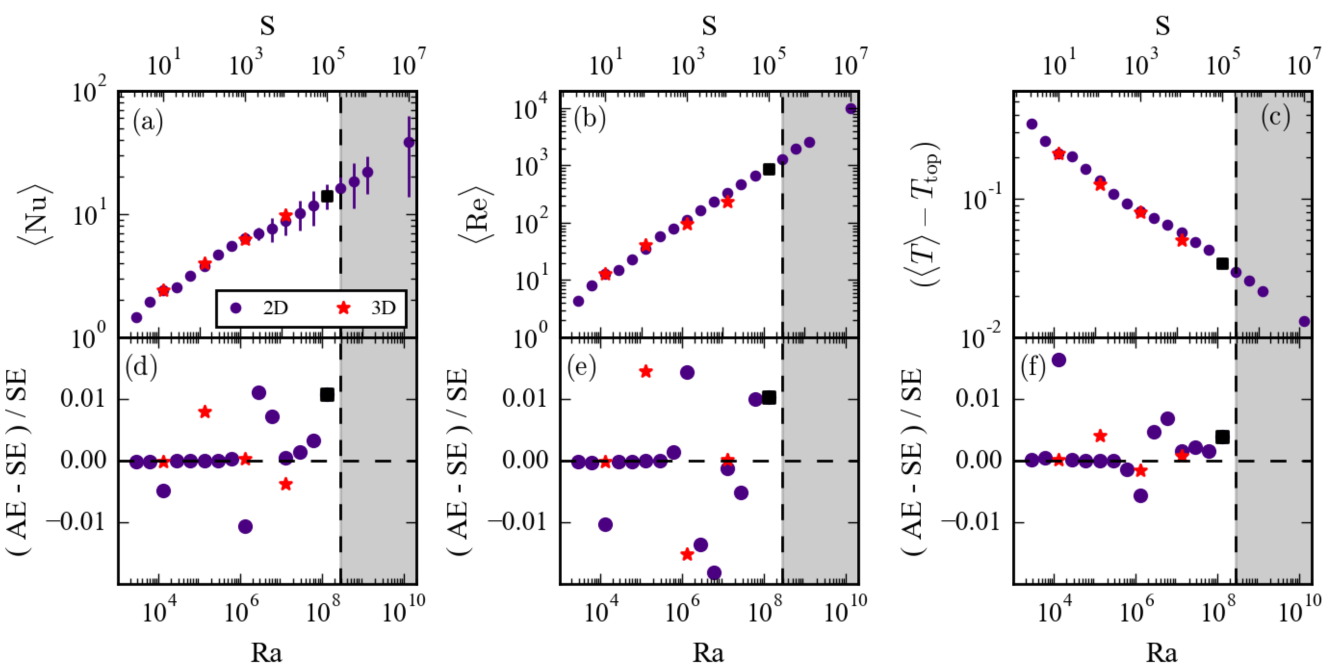

FIG. 3. Volume- and time-averaged measurements of the Nusselt number (Nu), the RMS Reynolds number (Re), and the mean temperature ($\langle T\rangle$) for AE runs are shown in (a)-(c). Symbols are located at the mean value of each measurement and denote 2D (purple circles) and 3D (red stars). The run at $S = 10^5$ marked as a black square is examined in more detail in Figs. 1, 2, 4, & 5. Vertical lines represent the standard deviation of the measurement, and quantify natural variation over the averaging window. (a) Nu scales as $\mathrm{Ra}^{1/5}$; above $\mathrm{S} \geq 10^{3+2/3}$, simulations exhibit oscillating plume structures whose heat transport fluctuates over time as a result of temporally-varying entrainment of wrongly signed temperature perturbations (see Fig. 2). (b) Re, which measures the level of turbulence in the evolved solution, scales as $\mathrm{Ra}^{0.45}$. (c) The difference between $\langle T\rangle$ and the value of T at $z = +1/2$ is shown, and this quantity scales as $\mathrm{Ra}^{-1/5}$, the inverse of Nu. Relative error for measurements of (d) Nu, (e) Re, and (f) T between AE solutions and SE solutions are shown. The greyed area of the plots indicates the region in which only AE runs were carried out due to computational expense.

marginally greater error, with AE measurements being $\leq 2\%$ different from SE measurements.

The measurements presented in Fig. 3 demonstrate that AE can be powerfully employed in parameter space studies in which large numbers of simulations are compared in a volume-averaged sense. We now turn our examination to a more direct comparison of AE and SE for convection at $S = 10^5$, the time and flux evolution of which was shown in Fig. 1. All comparisons that follow for these two runs occur over the times shaded in green in Fig. 1a&c. Measurements are sampled every 0.1 freefall time units for 500 total time units.

As AE is fundamentally a 1D adjustment to the thermodynamic structure of the solution, we compare the horizontally- and time-averaged temperature profiles attained by AE and SE in Fig. 4a. The boundary layer width and structure are nearly identical between the two solutions, but the the mean temperature in the isothermal interior differs by roughly 0.5% (Fig. 4c).

The probability distribution functions (PDFs) of point-by-point temperature measurements are compared for the two runs in Fig. 4b. To construct these PDFs, we interpolate the temperature field of each of these snapshots onto an evenly spaced grid, determine the frequency distribution of all measured T values, and then normalize the distribution such that its integral is unity. The two PDFs have noticeably different modes, as is expected from Fig. 4a. Over long timescales, the 0.5% difference between the two profiles would disappear, as the AE solution evolves to be exactly the SE solution – this is evident in the asymmetry of the AE PDF near the mode in Fig. 4b and also the trend of the mean temperature over time in Fig. 1c.

One means of comparing two PDFs to determine if they are drawn from the same underlying sample distribution is through the use of a Kolmogorov-Smirnov (KS) test [25]. We calculate the KS statistic for a PDF of some value, q, as

$$\mathrm{KS}(q) = \mathrm{CDF}_{\mathrm{AE}}(q) - \mathrm{CDF}_{\mathrm{SE}}(q), \tag{13}$$

where CDF stands for cumulative distribution function, the integral of the PDF. A traditional Kolmogorov-Smirnov statistic is just a single value, $\overline{\mathrm{KS}(q)} = |\mathrm{KS}(q)|_\infty = \max|\mathrm{KS}(q)|$, and we use both the profile $\mathrm{KS}(q)$ and $\overline{\mathrm{KS}(q)}$ to gain insight into the likeness of two PDFs. We show the KS profile in Fig. 4d, and the CDFs used to construct it overlay the PDFs in Fig. 4b. Near the modes of the temperature PDFs, the $\overline{\mathrm{KS}(T)} = 0.495$, which is very large and implies that roughly half of all temperature measurements in the SE case are greater than those in the AE case. This difference is significant, and shows that the two PDFs are distinctly different, but aside from this large value near the modes the KS profile has very small values, indicating that the temperature fluctuations away from the modes in the

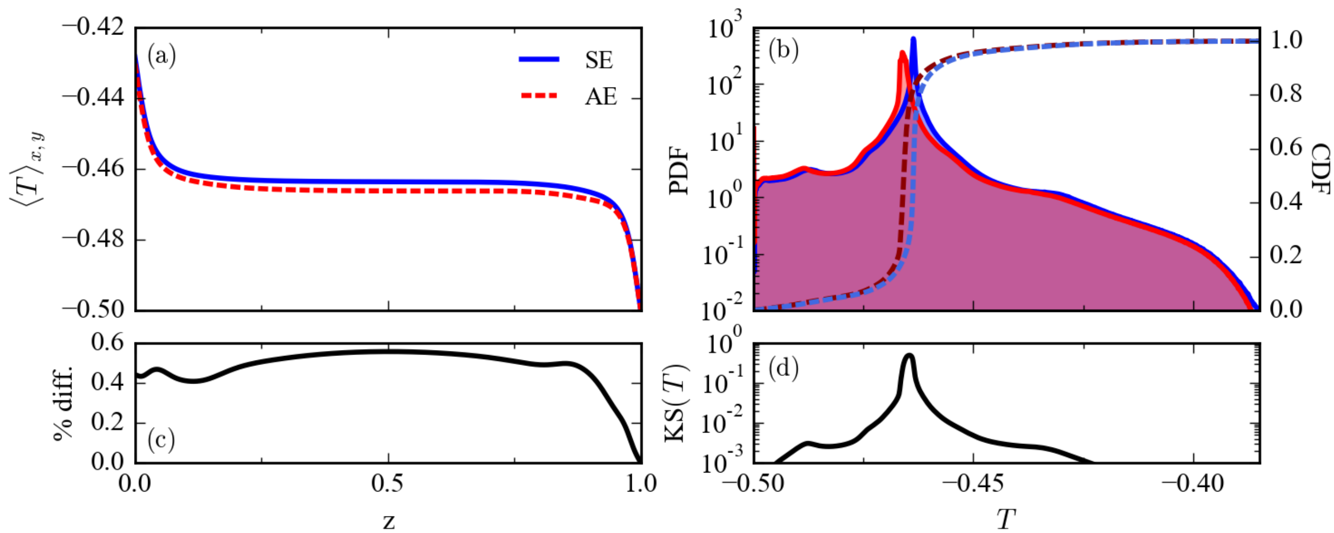

FIG. 4. Comparisons of the evolved thermodynamic states of an AE and SE run at $S = 10^5$ are shown. (a) Evolved horizontally- and time-averaged temperature profiles, as a function of height. (b) Probability Distribution Functions (PDFs) and their integrated Cumulative Distribution Functions (CDFs) of point-by-point measurements of the temperature field. (c) The percentage difference between the mean temperature profiles as a function of height. The difference between the mean profiles is very small, O(0.5%). (d) The value of the Kolmogorov-Smirnov (KS) statistic, or the difference between the AE and SE CDFs, as a function of temperature. The small difference in the interior temperature results in a large difference between the two temperature CDFs near the values of the temperature modes. The spread of temperature around the modes, which includes the fluctuations that drive convection, are nearly identical between the two runs.

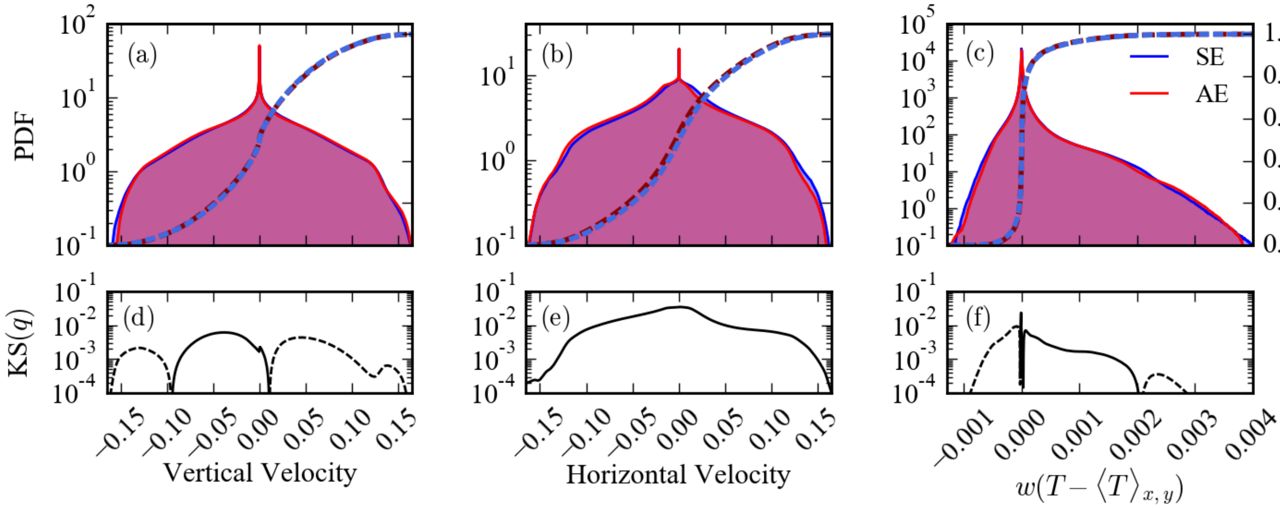

FIG. 5. Probability distribution functions (PDFs) of (a) the vertical velocity, (b) the horizontal velocity, and (c) nonlinear convective transport are shown for 2D runs achieved through SE (blue) and AE (red) at $S = 10^5$. The cumulative distribution function (CDF) is overplotted for each PDF. (d-f) The KS statistics, or the values of $\mathrm{CDF_{AE}}$ - $\mathrm{CDF_{SE}}$, are shown for the related distributions, and solid lines indicated positive values while dashed lines are negative values. Unlike the temperature distributions in Fig. 4, these distributions, particularly the vertical velocity and transport, show very good agreement and small values of the KS statistic.

two cases are nearly identical.

In addition to comparing the thermodynamic state achieved by the SE and AE methods, we examine the velocities found in the evolved states. Shown are the PDFs of vertical velocity (Fig. 5a), horizontal velocity (Fig. 5b), and the nonlinear vertical convective flux (Fig. 5c). The CDFs of each profile are overplotted, and corresponding KS profiles are shown in Fig. 5d-f. We report $\overline{\mathrm{KS}(w)} = 0.00615$ (vertical velocity), $\overline{\mathrm{KS}(u)} = 0.0349$ (horizontal velocity), and $\overline{\mathrm{KS}(w(T - \langle T\rangle_{x,y}))} = 0.0263$. Each PDF here shows a strong peak near zero due to the no-slip, impenetrable velocity boundary conditions (Eqn. (7)). The difference in vertical velocity and heat transport between AE and SE is negligible, which is unsurprising in light of the Nu measurements of Fig. 3a&d. The horizontal velocity shows some small deviation between the two simulations, and this likely relates to the nature of the strength of the horizontally oscillatory motions as we previously described in the context of suppressed Nu scaling. Thus, while the temperature profiles are distinctly drawn from different distributions in Fig. 4b, the profiles are similar enough that they drive nearly identical nonlinear dynamics.

The small differences between the SE and AE solutions for the case studied in Figs. 1, 4, & 5, show the extreme power of AE. In addition to the fact that AE runs require much less total simulation time (see e.g., Fig. 1a&c and the time values in the green highlighted regions), the first application of AE in a given simulation (Fig. 1c, at the arrow labeled "1") drastically increases the average timestep by immediately progressing the simulation into a more converged state. For the $S = 10^5$ case we examined in detail, the average time step size grew by a factor of 2-3 due to the decreased convective velocities from the transient state to the evolved state. At $S = 10^7$, the AE solve immediately improved the timestep size by nearly a factor of 4. Thus, AE achieves converged solutions in few simulation time units, while also taking less real world time per simulation time unit, when compared to the slowly converging SE state at the same simulation time.

IV. EXTENSIONS & CONCLUSIONS

In this work we have studied a method of Accelerated Evolution (AE) which can be employed to achieve rapid thermal convergence of convective simulations. We compared this technique to the Standard Evolution (SE) of convection through a thermal diffusion timescale and showed that AE rapidly obtains solutions whose dynamics are similar to SE solutions. The AE method is not only valid at low values of S, where SE solutions converge quickly due to the short thermal timescale, but AE is also applicable at high values of S, where SE solutions are intractable. As discussed, 2D and 3D are identical short of the time-varying entrainment states (Fig. 2), so we have restricted most of our study to 2D. However, due to the greater computational expense of 3D runs, they stand to gain more time savings from AE. This is a sentence about the magnitude of savings involved for AE vs. SE (wall time + cpu hours, 2d: 10^5, 3d: 10^4).

Here we studied Rayleigh-Bénard convection as a test case for the AE method, but we argue that the true power of this technique is in its extensions to more complicated studies. To achieve AE in more complicated systems, one need only derive the steady-state, horizontally-averaged equations governing the convective dynamics (e.g., Eqns. (10) & (11)) and couple those equations with knowledge of the boundary conditions and current dynamics as described in section II A and appendix A. While in-depth studies of AE extensions are beyond the scope of this paper, we will briefly discuss avenues in which the AE method should be explored and tested.

Convection in natural systems is often driven by internal heating processes rather than imposed, fixed boundary conditions. The AE procedure can be straightforwardly applied to Boussinesq studies of internally heated convection [26], where a constant source term in the energy equation causes the vertical flux through the system to increase with height. These systems can be studied using exactly the methods that we examined here, but multiplying the flux profiles derived in Eqn. (8) by the proper, height-dependent flux. Studies of convection in natural system often employ height-dependent conductivities [27, 28], leading to natural flux divergences that act as internal heating terms. The study of AE in the context of simple internal heating simulations will be an important step towards achieving AE in simulations with astrophysically realistic conductivities.

A further area which could benefit from AE is overshooting convection, in which studies examine adjacent stable and convecting regions [13, 14, 16]. When the interface between the stable region and the convecting region is stiff and motions do not cross that interface, convective motions cannot accelerate the restratification of the stable region. In fully-convective domains, such as those studied in this work, the thermodynamics evolve at a more rapid rate than the thermal diffusion time across the domain due to convective mixing. For example, in Fig. 1a, the SE solution is fully converged after $4 \cdot 10^3$ frefall time units, despite the thermal timescale being roughly 10^4 freefall units. However, in studies where there is a stable region which is not mixed by convection, the experimentalist must either wait through a thermal diffusion time for the region to restratify or employ other methods [13] to study evolved atmospheres.

Studies of stratified, compressible convection have much to gain through developing and employing AE. In many studies of stratified convection, the thermal diffusivity is inversely proportional to the density [7]. Thus, the thermal timescale grows with depth in the atmosphere, and the difficulty of achieving thermal convergence grows as simulators study more highly stratified domains. In order to extend AE into this regime, two additional pieces of information must be considered. First, rather than constructing the profiles in Eqn. (8) with the total flux through the domain, only the superadiabatic portion of the flux should be considered. Second, in addition to solving for hydrostatic balance and thermal equilibrium, as in Eqns. (10) & (11), it is essential to simultaneously evolve the density profile in a manner which conserves mass. In a 1D boundary value problem, such as is solved to achieve AE here, this implies the inclusion of an equation which tracks the vertically integrated mass, and sets boundary conditions on that mass to ensure that no mass enters or leaves the domain. [GIVE NUMBERS]

An eventual use case of AE is in robustly describing convection in stellar evolution codes. Current state of the art stellar structure models are the solutions of 1D simulations which parameterize convection using Mixing Length Theory [29]. Recent work has taken first steps towards understanding how to simultaneously resolve convective motions while evolving systems through many thermal timescales, as is required when modeling the evolution of stars over the course of stellar lifetimes. We now know that implicit timestepping methods, while not technically bound by CFL constraints, must resolve the convective motions for stability [3–5], and are thus not an ideal solution to achiving long-term system evolution. Recently, efforts have begun to project the results of 3D simulations into 1D models to more properly parameterize convection for stellar evolution [30, 31]. Through the careful addition and testing of new physics, AE can be generally applied to very large complex problems such as stellar evolution, and shows great potential for improving our understanding of convection.

ACKNOWLEDGMENTS

EHA acknowledges the support of the University of Colorado's George Ellery Hale Graduate Student Fellowship. This work was additionally supported by NASA LWS grant number NNX16AC92G. Computations were conducted with support by the NASA High End Computing (HEC) Program through the NASA Advanced Supercomputing (NAS) Division at Ames Research Center on Pleiades with allocations GID s1647 and GID g26133.

Appendix A: Accelerated Evolution Recipe

In order to achieve Accelerated Evolution (AE), we pause the Direct Numerical Simulation (DNS) which is evolving the dynamics of convection and solve a 1D Boundary Value Problem (BVP) consisting of Eqns. (10) & (11). After solving this BVP, we appropriately adjust the fields being evolved in the DNS towards their evolved state, and then we continue running the now-evolved DNS. The specific steps taken in completing the AE method are as follows:

1. Wait some time, $t_{\text{transient}}$, before beginning the AE process.

2. During the DNS, calculate time averages of the 1D profiles of F_{conv}, F_{tot}, and $\langle \boldsymbol{u} \times \boldsymbol{\omega} \rangle_{x,y}$, updating them every timestep. To calculate these averages, we use a trapezoidal-rule integration in time, and then divide by the total time elapsed over which the average is taken.

3. Pause the DNS once the averages are sufficiently converged. To ensure that an average is converged, at least some time t_{min} must have passed since the average was started to ensure that the full range of convective dynamics are probed, and the profiles must change by no more than $P\%$ on a given timestep.

4. Construct $\text{F}_{\text{conv, ev}}$ and ξ as specified in section II A from the averaged profiles.

5. Solve the BVP for $\langle T_1 \rangle_{x,y}$ and $\langle \varpi \rangle_{x,y}$ of the evolved state. Set the horizontal average of the current DNS thermodynamic fields equal to the results of the BVP.

6. Multiply the velocity field and the temperature fluctuations, $T - \langle T \rangle_{x,y}$, by $\sqrt{\xi}$ in the DNS to properly reduce the convective flux.

7. Continue running the DNS

We refer to this process as an "AE BVP solve."

While the use of a single AE BVP solve rapidly advances the convecting state to one that is closer to the evolved state, we find that repeating this method multiple times is the best way to ensure that the AE solution is truly converged. For all runs in 2D at $S < 10^5$, we set $t_{\text{transient}} = 50$, completed an AE BVP solve with $t_{\text{min}} = 30$ and $P = 0.1$, and then repeated the procedure. For all 3D runs and 2D runs with $S \in [10^5, 10^6]$, we did a first AE BVP solve with $t_{\text{transient}} = 20$, $t_{\text{min}} = 20$, and $P = 1$ in order to quickly reach a near- converged state and vastly increase our timestep size. After this first solve, we completed two AE BVP solves, with $t_{\text{transient}} = 30$, $t_{\text{min}} = 30$, and $P = 0.1$ to get very close to the solution (as in Fig. 1c). At very high $S = 10^7$, we ran two AE BVP solves with $t_{\text{min}} = 20$ and $P = 1$. For the first solve, we set $t_{\text{transient}} = 20$, and for the second we set $t_{\text{transient}} = 30$. We used fewer solves at this high value of S in part to reduce the computational expense of the run, and in part because a third BVP generally did not greatly alter the solution (as in Fig. 1c, arrow 3). We wait 50 freefall times after the final AE BVP solve of each run before beginning to take measurements.

Appendix B: Table of Runs

In Table I we list key properties of all simulations conducted in this work.

[1] B. P. Brown, M. K. Browning, A. S. Brun, M. S. Miesch, and J. Toomre, "Persistent Magnetic Wreaths in a Rapidly Rotating Sun," Astrophys. J. **711**, 424–438 (2010), arXiv:1011.2831 [astro-ph.SR].

[2] N. A. Featherstone and B. W. Hindman, "The Spectral Amplitude of Stellar Convection and Its Scaling in the High-Rayleigh-number Regime," Astrophys. J. **818**, 32 (2016), arXiv:1511.02396 [astro-ph.SR].

[3] M. Viallet, I. Baraffe, and R. Walder, "Towards a new generation of multi-dimensional stellar evolution models: development of an implicit hydrodynamic code," Astronomy & Astrophysics **531**, A86 (2011), arXiv:1103.1524 [astro-ph.IM].

[4] M. Viallet, I. Baraffe, and R. Walder, "Comparison of different nonlinear solvers for 2D time-implicit stellar hydrodynamics," Astronomy & Astrophysics **555**, A81 (2013), arXiv:1305.6581 [astro-ph.SR].

[5] M. Viallet, T. Goffrey, I. Baraffe, D. Folini, C. Geroux, M. V. Popov, J. Pratt, and R. Walder, "A Jacobian-free Newton-Krylov method for time-implicit multidimensional hydrodynamics. Physics-based preconditioning for sound waves and thermal diffusion," Astronomy & Astrophysics **586**, A153 (2016), arXiv:1512.03662 [astro-ph.IM].

[6] D. Lecoanet, B. P. Brown, E. G. Zweibel, K. J. Burns, J. S. Oishi, and G. M. Vasil, "Conduction in Low Mach Number Flows. I. Linear and Weakly Nonlinear Regimes," Astrophys. J. **797**, 94 (2014), arXiv:1410.5424 [astro-ph.SR].

[7] E. H. Anders and B. P. Brown, "Convective heat transport in stratified atmospheres at low and high Mach number," Physical Review Fluids **2**, 083501 (2017), arXiv:1611.06580 [physics.flu-dyn].

[8] B. Bordwell, B. P. Brown, and J. S. Oishi, "Convective Dynamics and Disequilibrium Chemistry in the Atmospheres of Giant Planets and Brown Dwarfs," Astrophys. J. **854**, 8 (2018), arXiv:1802.03026 [astro-ph.EP].

[9] M. Stix, "On the time scale of energy transport in the sun," Solar Physics **212**, 3–6 (2003).

TABLE I. Simulation parameters. We report the supercriticality (S), Rayleigh number (Ra), and coefficient resolution (nz, nx, and ny are the number of coefficients in the z, x, and y directions respectively). Simulation run times required to reach convergence are reported for the SE solutions ($t_{\rm therm}$) and the AE solutions ($t_{\rm AE}$). The amount of time over which simulations measurements were taken in the evolved state is listed ($t_{\rm avg}$). All times are in freefall time units. The volume-averaged Nusselt number (Nu) of the AE and SE solutions are shown. In the upper part of the table, information pertaining to 2D runs is reported, and below the double horizontal bars we report properties of all 3D runs.

S	Ra	nz	nx, ny	$t_{\rm therm}$	$t_{\rm AE}$	$t_{\rm avg}$	$\mathrm{Nu}_{\rm SE}$	$\mathrm{Nu}_{\rm AE}$
				2D Runs				
$10^{1/3}$	$2.79 \cdot 10^3$	32	64	52.8	340	100	1.46	1.46
$10^{2/3}$	$6.01 \cdot 10^3$	32	64	77.6	282	100	1.95	1.95
10^{1}	$1.30 \cdot 10^4$	32	64	114	265	100	2.43	2.42
$10^{1+1/3}$	$2.79 \cdot 10^4$	32	64	167	251	100	2.54	2.54
$10^{1+2/3}$	$6.01 \cdot 10^4$	32	64	245	245	100	3.14	3.14
10^{2}	$1.30 \cdot 10^5$	64	128	360	326	100	3.8	3.8
$10^{2+1/3}$	$2.79 \cdot 10^5$	64	128	528	248	100	4.71	4.71
$10^{2+2/3}$	$6.01 \cdot 10^5$	64	128	776	251	100	5.5	5.5
10^{3}	$1.30 \cdot 10^6$	128	256	$1.14 \cdot 10^3$	268	200	6.4	6.33
$10^{3+1/3}$	$2.79 \cdot 10^6$	128	256	$1.67 \cdot 10^3$	247	500	6.87	6.95
$10^{3+2/3}$	$6.01 \cdot 10^6$	256	512	$2.45 \cdot 10^3$	275	500	7.54	7.59
10^{4}	$1.30 \cdot 10^7$	256	512	$3.60 \cdot 10^3$	301	500	8.83	8.83
$10^{4+1/3}$	$2.79 \cdot 10^7$	256	512	$5.28 \cdot 10^3$	317	500	10.13	10.14
$10^{4+2/3}$	$6.01 \cdot 10^7$	256	512	$7.76 \cdot 10^3$	326	500	11.65	11.69
10^{5}	$1.30 \cdot 10^8$	512	1024	$1.14 \cdot 10^4$	411	500	14.02	14.18
$10^{5+1/3}$	$2.79 \cdot 10^8$	512	1024	$1.67 \cdot 10^4$	391	500	—	16.21
$10^{5+2/3}$	$6.01 \cdot 10^8$	512	1024	$2.45 \cdot 10^4$	453	500	—	18.58
10^{6}	$1.30 \cdot 10^9$	1024	2048	$3.60 \cdot 10^4$	436	500	—	22.13
10^{7}	$1.30 \cdot 10^{10}$	2048	4096	$1.14 \cdot 10^5$	183	170	—	38.29
				3D Runs				
10^{1}	$1.30 \cdot 10^4$	32	64×64	114	261	100	2.42	2.42
10^{2}	$1.30 \cdot 10^5$	64	128×128	360	249	100	3.97	4
10^{3}	$1.30 \cdot 10^6$	128	256×256	$1.14 \cdot 10^3$	243	500	6.27	6.27
10^{4}	$1.30 \cdot 10^7$	256	512×512	$3.60 \cdot 10^3$	244	500	9.92	9.88

[10] H. Johnston and C. R. Doering, "Comparison of Turbulent Thermal Convection between Conditions of Constant Temperature and Constant Flux," Phys. Rev. Lett. **102**, 064501 (2009), arXiv:0811.0401 [physics.flu-dyn].

[11] R. Verzicco and R. Camussi, "Transitional regimes of low-Prandtl thermal convection in a cylindrical cell," Physics of Fluids **9**, 1287–1295 (1997).

[12] N. E. Hurlburt, J. Toomre, and J. M. Massaguer, "Two-dimensional compressible convection extending over multiple scale heights," Astrophys. J. **282**, 557–573 (1984).

[13] L.-A. Couston, D. Lecoanet, B. Favier, and M. Le Bars, "Dynamics of mixed convective-stably-stratified fluids," Physical Review Fluids **2**, 094804 (2017), arXiv:1709.06454 [physics.flu-dyn].

[14] A. Brandenburg, K. L. Chan, Å. Nordlund, and R. F. Stein, "Effect of the radiative background flux in convection," Astronomische Nachrichten **326**, 681–692 (2005), astro-ph/0508404.

[15] R. J. A. M. Stevens, D. Lohse, and R. Verzicco, "Prandtl and Rayleigh number dependence of heat transport in high Rayleigh number thermal convection," Journal of Fluid Mechanics **688**, 31–43 (2011), arXiv:1102.2307 [physics.flu-dyn].

[16] N. E. Hurlburt, J. Toomre, and J. M. Massaguer, "Nonlinear compressible convection penetrating into stable layers and producing internal gravity waves," Astrophys. J. **311**, 563–577 (1986).

[17] E. A. Spiegel and G. Veronis, "On the Boussinesq Approximation for a Compressible Fluid." Astrophys. J. **131**, 442 (1960).

[18] F. Cattaneo, N. H. Brummell, J. Toomre, A. Malagoli, and N. E. Hurlburt, "Turbulent compressible convection," Astrophys. J. **370**, 282–294 (1991).

[19] L. Korre, N. Brummell, and P. Garaud, "Weakly non-Boussinesq convection in a gaseous spherical shell," Phys. Rev. E **96**, 033104 (2017), arXiv:1704.00817 [physics.flu-dyn].

[20] K. Burns, G. Vasil, J. Oishi, D. Lecoanet, and B. Brown, "Dedalus: Flexible framework for spectrally solving differential equations," Astrophysics Source Code Library (2016), ascl:1603.015.

[21] U. M. Ascher, S. J. Ruuth, and R. J. Spiteri, "Implicit-explicit Runge-Kutta methods for time-dependent partial differential equations," Applied Numerical Mathematics **25**, 151–167 (1997).

[22] David Goluskin, Hans Johnston, Glenn R. Flierl, and Edward A. Spiegel, "Convectively driven shear and decreased heatflux," J. Fluid Mech. **759**, 360–385 (2014).

[23] Guenter Ahlers, Siegfried Grossmann, and Detlef Lohse, "Heat transfer and large scale dynamics in turbulent rayleigh-bénard convection," Rev. Mod. Phys. **81**, 503–537 (2009).

[24] J. Otero, R. W. Wittenberg, R. A. Worthing, and C. R. Doering, "Bounds on Rayleigh Bénard convection with an imposed heat flux," J. Fluid Mech. **473**, 191–199 (2002).

[25] J. V. Wall and C. R. Jenkins, *Practical Statistics for Astronomers, by J. V. Wall , C. R. Jenkins, Cambridge, UK: Cambridge University Press, 2012* (2012).

[26] David Goluskin, *Internally Heated Convection and Rayleigh-Bénard Convection* (Springer International Publishing, 2016).

[27] A. Brandenburg, "Stellar Mixing Length theory with entropy rain," arXiv (2016), arXiv:1504.03189.

[28] P. J. Käpylä, M. Rheinhardt, A. Brandenburg, R. Arlt, M. J. Käpylä, A. Lagg, N. Olspert, and J. Warnecke, "Extended Subadiabatic Layer in Simulations of Overshooting Convection," Astrophys. J. Lett. **845**, L23 (2017), arXiv:1703.06845 [astro-ph.SR].

[29] B. Paxton, L. Bildsten, A. Dotter, F. Herwig, P. Lesaffre, and F. Timmes, "Modules for Experiments in Stellar Astrophysics (MESA)," The Astrophysical Journal Supplement Series **192**, 3 (2011), arXiv:1009.1622 [astro-ph.SR].

[30] W. D. Arnett, C. Meakin, M. Viallet, S. W. Campbell, J. C. Lattanzio, and M. Mocák, "Beyond Mixing-length Theory: A Step Toward 321D," Astrophys. J. **809**, 30 (2015), arXiv:1503.00342 [astro-ph.SR].

[31] A. Cristini, C. Meakin, R. Hirschi, D. Arnett, C. Georgy, and M. Viallet, "Linking 1D evolutionary to 3D hydrodynamical simulations of massive stars," Physica Scripta **91**, 034006 (2016), arXiv:1601.01572 [astro-ph.SR].